Activation of anomalous Hall effect and orbital magnetization by domain walls in altermagnets

Sopheak Sorn [1,2,*] and Yuriy Mokrousov [3,4]

[1] Institute for Quantum Materials and Technology, Karlsruhe Institute of Technology, 76131 Karlsruhe, Germany
[2] Institute of Theoretical Solid State Physics, Karlsruhe Institute of Technology, 76131 Karlsruhe, Germany
[3] Peter Grünberg Institut (PGI-1), Forschungszentrum Jülich, 52425 Jülich, Germany
[4] Institute of Physics, Johannes Gutenberg University Mainz, 55099 Mainz, Germany

(Received 31 May 2025; revised 3 October 2025; accepted 5 November 2025; published 5 December 2025)

Altermagnets are an emerging class of unconventional antiferromagnets, characterized by a Néel ordering that does not break the translational symmetry of the underlying lattice. Depending on the orientation of the Néel vector, the anomalous Hall effect (AHE) may or may not exist. In the so-called pure altermagnets, the AHE is forbidden by magnetic symmetry. Here, we demonstrate that in pure altermagnets, domain walls can lift the symmetry constraints, thereby activating the AHE and orbital magnetization. Taking a representative example of a rutile-lattice tight-binding minimal model in slab geometry, we use linear response theory to demonstrate the emergence of the domain-wall AHE, finding that it is closely related to the orbital magnetization, while the spin magnetization does not play a significant role. Using Landau theory, we argue that, while for a random arrangement of π domain walls, the contributions from the individual domain walls will cancel one another, an external magnetic field will favor domain-wall arrangements with specific chirality giving rise to a net AHE signal. Using group theory, we discuss how these findings can be straightforwardly generalized to certain other classes of altermagnets. Our work reveals a crucial role for domain walls in understanding Hall transport and orbital magnetism of altermagnets. Our work generally calls for a rigorous analysis of Hall-transport data for an altermagnet, ideally in conjunction with imaging data, in order to unambiguously assign an observed Hall effect to magnetic domains or to domain walls.

DOI: 10.1103/vzmh-mxlz

I. INTRODUCTION

Recent developments in the field of magnetism have uncovered a new class of unconventional antiferromagnets, known as altermagnets, wherein a Néel ordering together with unusual crystal symmetry plays a crucial role in dictating many physical properties [1–3]. In an altermagnet, sublattices in each unit cell are divided into two sets based on the direction of the staggering local dipole moments that define the Néel vector. A defining feature that distinguishes an altermagnet from a conventional antiferromagnet is the way the two sets of sublattices can be interchanged, neither by translation nor inversion, but by other symmetry operations such as rotation. This prevents Kramers' degeneracy in the electronic band structures and results in a momentum-dependent band splitting, which finds applications in spintronics and drives intense research activity [1–8].

Because of spin-orbit coupling (SOC), the Néel vector is commonly locked into an easy-axis direction. In the so-called pure altermagnets, the easy axis lies in a high-symmetry direction such that the anomalous Hall effect (AHE) is forbidden by symmetry [9]. Since a net magnetization shares the same symmetry properties as the AHE, a magnetic dipole-like order parameter can be ruled out. Restricting to centrosymmetric systems, the inversion symmetry also prevents order parameters that behave like magnetic quadrupole moments [10–13]. The order parameters turn out to be higher-ranked magnetic multipole moments such as magnetic octupoles and magnetic hexadecapoles [9,14–16]. Notable implications of the magnetic multipolar nature of the order parameters include the emergence of nodal-line structures in the electronic bands [9,17–19] and characteristic nonlinear response properties [20–23]. For instance, magnetic octupolar order parameters lead to a third-order Hall response and a second-order magneto-electric effect, while lower orders of these effects are absent [20,22,23]. Closely related to the magnetic octupolar order are such phenomena as piezomagnetism, strain-induced AHE, and unusual couplings to strain fields [14,16,24,25]. In contrast, when the easy axis lies in a lower-symmetry direction, the symmetry can allow for a nontrivial AHE as well as a nonzero macroscopic magnetic dipole moment—equivalently a net magnetization [26–32]. The latter arises from the mechanism of a weak ferromagnetism, and its magnitude can be small. Such altermagents have been referred to as mixed altermagnets since ferromagnetic-like order parameters are present [9]. Recently, it was argued that in some classes of altermagnets, in particular those with rutile structure, the weak magnetism is dominated by g-tensor anisotropy and the corresponding anisotropy of orbital magnetism, with weak magnetization dominated by orbital contributions [33].

*Contact author: sopheak.sorn@kit.edu

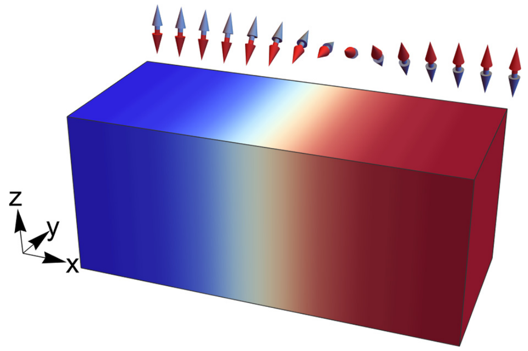

FIG. 1. Geometrical setup of a film periodic in the yz plane featuring an open boundary condition along the x axis. The double-sided arrows denote local Néel vectors that form a Bloch-type domain wall along x.

In this paper, we investigate Hall transport in altermagnets in the presence of magnetic domain walls (DWs), which are ubiquitous in actual settings yet have received less attention [18,34]. We focus on pure altermagnets where the AHE is absent in the absence of DWs, so that if the AHE is activated, it is obviously attributed to the DWs. We study this using a rutile-lattice tight-binding model in a slab geometry and coupling electrons to a Bloch-type DW of the Néel vector as schematically shown in Fig. 1. The double-headed arrows denote the local Néel vectors, each of which is associated with the two antiparallel local dipole moments residing on the A and B sublattices of the rutile lattice in Fig. 2. These local dipole moments are denoted by the blue and red arrows. We assume translational invariance in the slab plane; thus, the Néel vector profile corresponds to an infinite DW plane. We use the Kubo formula to compute the Hall conductivity for the slab geometry and find that the DW indeed activates the AHE. AHE with a similar DW-dominated origin has been observed very recently for the first time in a layered collinear antiferromagnet $EuAl_2Si_2$ [35]. This is in contrast to DWs in ferromagnets, which commonly play a supplementary role since the magnetic domains can also have a nontrivial AHE contribution [36–38].

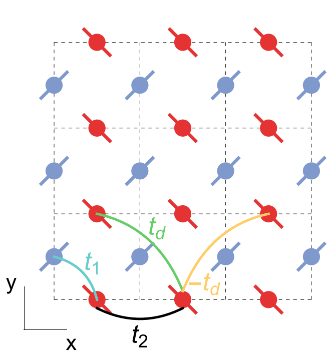

FIG. 2. A representation of a rutile lattice featuring the magnetic sublattices, A (blue dots) and B (red dots). The A and the B sublattices reside on different xy planes and experience different local potentials because of cages of nonmagnetic atoms (not shown), whose orientation is shown with tilted line segments.

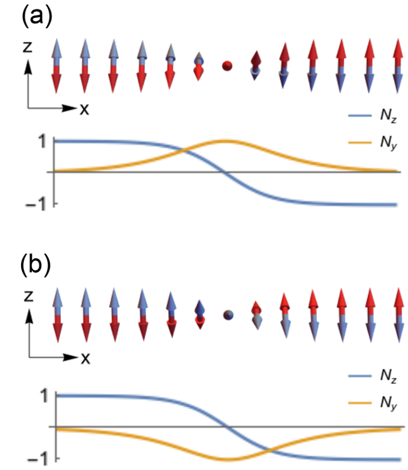

FIG. 3. Illustration of Bloch-type DWs of the Néel vector $\vec{N}(\vec{x})$. The orientation of the local Néel vector is given by $\vec{N} = \frac{1}{2}(\vec{m}_{\text{blue}} - \vec{m}_{\text{red}})$, where $\vec{m}_{\text{blue,red}}$ denote the orientation of the local magnetic dipole moments that occupy the A and the B sublattices, respectively. Panels (a) and (b) correspond to opposite chiralities. The bottom plots show the profiles of $N_{y,z}(\vec{x})$. In the presence of an inversion symmetry, the two chiralities are energetically degenerate.

We find that within our model for a uniform bulk and for the easy-axis direction of $\vec{N}$ corresponding to a mixed altermagnet, the orbital magnetization is by far greater than the weak spin ferromagnetism. In contrast, our analysis of the DW impact on the orbital and spin magnetization shows that they exhibit a similar order of magnitude. Nonetheless, the computations reveal a strong connection between the orbital magnetization and the DW AHE: the Hall conductivity is most dominant in the plane perpendicular to the orbital magnetization. Meanwhile, the spin magnetization lies predominantly in the Hall plane. This means that the orientation of the spin magnetization predicts the wrong Hall plane for which the Hall effect is the strongest. Because of inversion symmetry, the DWs of opposite chirality are energetically degenerate (see Fig. 3). The AHE because of the latter has a canceling effect on that owing to the former. As a result, when we consider profiles with multiple DWs, a random arrangement of DWs with equal populations of opposite chiralities is expected to yield a trivial AHE. However, using Landau theory for altermagnets, we argue that an external magnetic field favors a specific chirality population, and the AHE contributions from individual DWs accumulate rather than cancel one another. Meanwhile, the magnetic domains themselves are less affected because of the magnetic multipolar nature of the order parameter, which couples to the external field only at the third order, whereas the coupling with the DW chirality takes place at the linear order. Finally, we use a group theoretical framework to generalize our results for the rutiles to other classes of pure altermagnets.

This manuscript is organized as follows. In Sec. II, we introduce the rutile-lattice tight-binding model and study the band structure, the Hall conductivity, the orbital magnetization, and the spin magnetization in the collinear bulk when DWs are absent. Section III introduces a DW Ansatz in the slab geometry and discusses the Hall conductivity, the orbital magnetization, and the spin magnetization induced by the DW. We also elucidate how, in multi-DW textures, AHE contributions from individual DWs may accumulate or cancel out one another. Section IV discusses insights from a Landau theory for altermagnets on how an external field can select a chirality population in multi-DW textures and thus result in a nontrivial DW AHE. In Sec. V, we present a group-theoretical analysis, which shows how our results for the rutile altermagnetic model can be generalized to other classes of altermagnets. Section VI is the summary.

II. MODEL

In this section, we introduce the tight-binding model and then analyze the band structure, the Hall conductivity, the orbital magnetization, and the spin magnetization for the collinear bulk [39] featuring a uniform Néel vector $\vec{N}$. These provide helpful insight for when we study the impact of DWs later.

We consider a single-orbital tight-binding model on a rutile lattice, as shown in Fig. 2. In reciprocal space and with the basis $(a_{\vec{k}\uparrow}, a_{\vec{k}\downarrow}, b_{\vec{k}\uparrow}, b_{\vec{k}\downarrow})^T$ of the annihilation operators, the Bloch Hamiltonian is given by [17,18,40]

$$\mathcal{H} = \mathcal{H}_0 + \mathcal{H}_{\text{soc}}, \tag{1}$$

$$\begin{aligned}\mathcal{H}_0 = &-8t_1 c_{x/2}c_{y/2}c_{z/2}\tau_x - 2t_2' c_z\tau_0 - 2t_2(c_x + c_y)\tau_0 \\ &- 4t_d s_x s_y \tau_z + J\tau_z \vec{N}\cdot\vec{\sigma},\end{aligned} \tag{2}$$

$$\begin{aligned}\mathcal{H}_{\text{soc}} = &-8\lambda s_{z/2}(s_{x/2}c_{y/2}\sigma_x - s_{y/2}c_{x/2}\sigma_y)\tau_y \\ &+16\lambda' c_{x/2}c_{y/2}c_{z/2}(c_x - c_y)\tau_y\sigma_z,\end{aligned} \tag{3}$$

where $c_{\alpha/n} \equiv \cos(k_\alpha/n)$ and $s_{\alpha/n} \equiv \sin(k_\alpha/n)$. t_1, t_2, t_2', and t_d are hopping integrals for the processes illustrated in Fig. 2. λ and λ' are the SOC-enabled hoppings. τ_i's and σ_i's are Pauli matrices that act on the sublattice indices and the spin indices, respectively. We note that t_d, λ, and λ' are essential for altermagnetism since they originate in the distinct local environment of A and B sublattices. In the latter expressions, the Néel vector $\vec{N}$ is assumed to be spatially uniform. When $\vec{N}$ exhibits a texture, the real-space version of the model is employed. Without loss of generality, we assume that $\vec{N}$ is normalized.

Figures 4(a) and 4(b) show the band structure of the model for $\vec{N} = \hat{z}$ and $\vec{N} = \hat{y}$, respectively. As seen in (a), the band structure supports Weyl nodal lines, such as those along MA and ΓZ. On the $k_z = \pi$ plane, there are also Weyl nodal loops intersecting along AZ and manifesting as two band-crossing points. The symmetry protection of these Weyl nodal structures and their physical implications, e.g., the emergence of unconventional antichiral surface states, have been discussed in Refs. [17,18]. Particularly relevant for our AHE considerations is a Weyl nodal loop in the $k_z = \pi$ plane, which are protected by mirror $\mathcal{M}_z$ symmetry [17]. When $\vec{N} = \hat{y}$, the mirror protection is removed, and the band-crossing points are gapped out, as can be seen in Fig. 4(b). These anticrossings support a large concentration of local Berry curvature that results in a nontrivial dependence of the AHE on the chemical potential, as will be seen in Sec. II A. Compared with AZ, the Weyl nodal lines along ΓZ and MA seem to be intact upon

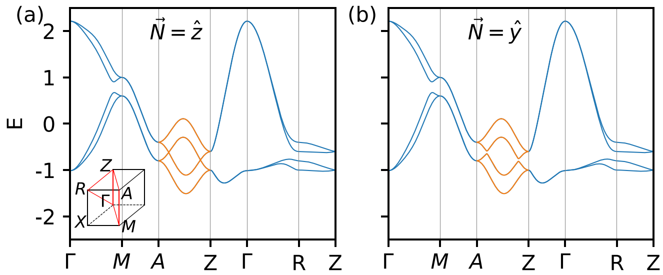

FIG. 4. Bulk band structures for (a) $\vec{N}_i = \hat{z}$ and (b) $\vec{N}_i = \hat{y}$. A notable distinction between the two panels is the band anticrossings along the AZ line, which is plotted in a different color. In (a), the band crossings along AZ are protected by z mirror and are a part of a Weyl nodal loop in the $k_z = \pi$ plane. In (b), the Néel vector lowers the symmetry, leading to the gap opening. The symmetry protection of the Weyl nodal lines such as those visible along ΓZ and MA, is discussed in the main text. The model parameters used are $t_1 = -0.2$, $t_2 = 0.025$, $t_2' = -0.35$, $t_d = 0.15$, $J = 0.2$, $\lambda = -0.025$, and $\lambda' = 0.0125$; see the main text.

the change in the direction of the Néel vector. A more detailed analysis reveals that, indeed, the Weyl nodal line along MA is protected by a combination of nonsymmorphic symmetry and an antiunitary symmetry (see Appendix A). However, the nodal line along ΓZ is not protected by any symmetry and can be gapped out by a symmetry-preserving perturbation (see Appendix A).

Anomalous Hall effect and orbital magnetization in collinear bulk

In this section, we will consider the AHE in the bulk with a fixed direction of the Néel vector, i.e., when the DWs are

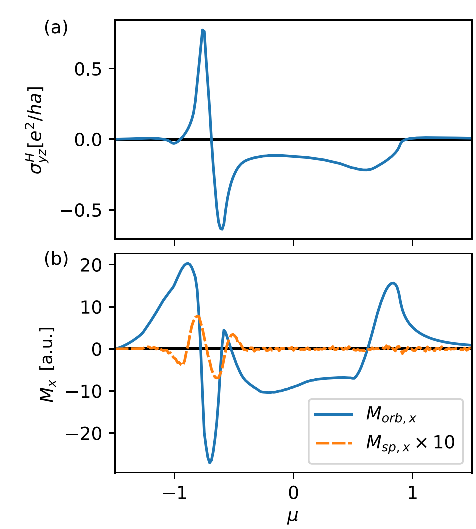

FIG. 5. The chemical potential dependence of the (a) Hall conductivity σ^H_{yz} and (b) orbital magnetization $M_{\text{orb},x}$ and spin magnetization $M_{\text{sp},x}$ for collinear bulk with $\vec{N} = \hat{y}$. Here, a is the length of the lattice vector along the direction perpendicular to the Hall plane. Note that the spin magnetization is multiplied with a factor of ten.

absent, for two cases: (i) $\vec{N} = \hat{z}$ and (ii) for $\vec{N} = \hat{y}$. Case (i) corresponds to a pure altermagnet, where AHE is forbidden by two mirror symmetries: $S_1 = \{\mathcal{M}_x|\frac{1}{2}\frac{1}{2}\frac{1}{2}\}$ and $S_2 = \{\mathcal{M}_z|000\}$. S_1 requires the time-reversal-odd Hall pseudovector $\vec{\sigma}_H = (\sigma^H_{yz}, \sigma^H_{zx}, \sigma^H_{xy})^T$ to be in the x direction, where σ^H_{ij} is the Hall conductivity in the ij plane. Meanwhile, S_2 requires $\vec{\sigma}_H$ to be in the z direction. As a result, $\vec{\sigma}_H = 0$.

On the other hand, in case (ii), S_2 is broken, while S_1 is still present. Therefore, only σ^H_{yz} is allowed to be nonzero. Since the average magnetization $\vec{M}$ is a time-reversal-odd pseudovector that transforms identically to $\vec{\sigma}_H$, its first component M_x is the only allowed component. Physically, it arises in rutile structure through the orbital mechanism of g-factor anisotropy [33]. Case (ii), therefore, is a mixed altermagnet. In the convention of Ref. [41], it corresponds to a canted altermagnet, where the small canting arises from the weak ferromagnetism.

We compute the Hall conductivity σ^H_{yz} from the k-dependent Berry curvature,

$$\sigma^H_{ij} = \frac{e^2}{\hbar}\sum_n \int \frac{d^3k}{(2\pi)^3} f(E_{\vec{k}n})\varepsilon_{ijl}\Omega_l(\vec{k}n), \tag{4}$$

where n is the band index, $f(E)$ is the Fermi-Dirac distribution function, ε_{ijl} is the Levi-Civita symbol, and $\vec{\Omega}(\vec{k}n)$ is the local Berry curvature. Figure 5(a) shows σ^H_{yz} as a function of the chemical potential μ. Near $\mu = -0.75$, σ^H_{yz} becomes pronounced and undergoes a sign change. This behavior is closely related to the band anticrossings on the ZA line in Fig. 4(b), which are associated with the gap opening of the Weyl nodal loops in Fig. 4(a). We have also checked that $\sigma^H_{xy} = \sigma^H_{zx} = 0$, consistent with the symmetry analysis.

We now compare the Hall conductivity for case (ii) with the spin magnetization $\vec{M}_{\text{spin}}$ and the orbital magnetization $\vec{M}_{\text{orb}}$ [42–45],

$$M_{\text{sp},i} = -\frac{e\hbar}{2}\sum_n \int \frac{d^3k}{(2\pi)^3} f(E_{\vec{k}n})\langle u_{\vec{k}n}|\sigma_i|u_{\vec{k}n}\rangle, \tag{5}$$

$$M_{\text{orb},i} = \frac{e\hbar}{2}\sum_n \sum_{m\neq n} \int \frac{d^3k}{(2\pi)^3} f(E_{\vec{k}n})(E_{\vec{k}n} + E_{\vec{k}m} - 2\mu) i\varepsilon_{ijl}\left[\frac{(v_j)^{nm}_{\vec{k}}(v_l)^{mn}_{\vec{k}} - (v_l)^{nm}_{\vec{k}}(v_j)^{mn}_{\vec{k}}}{(E_{\vec{k}n} - E_{\vec{k}m})^2}\right], \tag{6}$$

where we have assumed the spin g factor to be 2 and the unit such that the bare electron mass m_e is 1. v_j is the jth Cartesian component of the velocity operator, and its matrix element $(v_j)^{nm}_{\vec{k}}$ is given by $\langle u_{\vec{k}n}|\frac{1}{\hbar}\frac{\partial \mathcal{H}}{\partial k_j}|u_{\vec{k}m}\rangle$, where $|u_{\vec{k}m}\rangle$ is the Bloch eigenvector. For the choice of the hopping integrals, the effective mass of electrons is comparable with the bare mass, which allows a direct comparison between the numerical results for $M_{\text{orb},i}$ and $M_{\text{sp},i}$ [46].

Figure 5(b) shows a nontrivial μ dependence of $M_{\text{sp},x}$ (dashed orange line) and $M_{\text{orb},x}$ (solid blue line), which are the only nonzero components allowed by symmetry. Note that the spin magnetization data has been multiplied by a factor of 10. Our results reveal that the orbital contribution is dominant over the spin part. This strongly suggests the possibility of a dominant orbital magnetism in a mixed altermagnet in general.

In the rest of the paper, we study how a DW in a pure altermagnet effectively realizes the scenario in the pure case (i) away from the DW region while realizing a scenario akin to the mixed case (ii) within the DW region. As a result, a nonzero AHE and the concomitant orbital magnetization are activated and can be attributed solely to the DW.

III. ANOMALOUS HALL EFFECT FROM ALTERMAGNETIC DOMAIN WALLS

To study the AHE induced by altermagnetic DWs, we consider a Bloch DW of the Néel vector in the slab geometry as shown in Fig. 1. We consider the DW profile where the Néel vector in the ith unit cell is given by $\vec{N}_i$, for $-L_x/2 < i < L_x/2$, and L_x is the thickness of the slab. We use the following Ansatz for the Néel vector profile: $\vec{N}_i = (0, \sin\theta_i, \cos\theta_i)^T$. For the left-hand-side domain, $i \leqslant -w_{\text{dw}}/2$, $\theta_i = 0$, and for the right-hand-side domain $i \geqslant w_{\text{dw}}/2$, $\theta_i = \pi$. In the DW region, $-w_{\text{dw}}/2 < i < w_{\text{dw}}/2$, $\theta_i = \pi(2i + w_{\text{dw}})/2w_{\text{dw}}$, where w_{dw} characterizes the width of the DW. We then couple the conduction electrons hopping on the rutile-lattice slab geometry with this DW profile. Reference [18] studied the electronic spectrum in the presence of such DWs, uncovering the presence of unconventional bound states at the DWs. Here, we focus on how the DW gives rise to a nontrivial anomalous Hall response.

A. Anomalous Hall effect from altermagentic domain walls

We compute the DW Hall conductivity $\sigma^{H,DW}_{ij}$ in the presence of the DW using Kubo formula and the eigenvectors of the Hamiltonian matrix for the slab-geometry problem. The full expression for the Hall conductivity can be found in the Appendix B (see also Ref. [37]). We will only show the results for $\sigma^{H,DW}_{yz}$ and $\sigma^{H,DW}_{xy}$, since $\sigma^{H,DW}_{zx}$ is forbidden by the symmetry operation of twofold rotation C_{2y} followed by the time reversal and a fractional translation along the y-direction.

Figures 6(a) and 6(b) shows the chemical potential μ dependence of $\sigma^{H,DW}_{xy}$ and $\sigma^{H,DW}_{yz}$, respectively. We have used the same tight-binding parameters as in Sec. II, and we have chosen the film thickness $L_x = 100a$ and the DW width $w_{\text{dw}} = 20a$, where a is the length of the lattice vector. Our general observation is that $\sigma^{H,DW}_{yz}$ has a larger magnitude compared

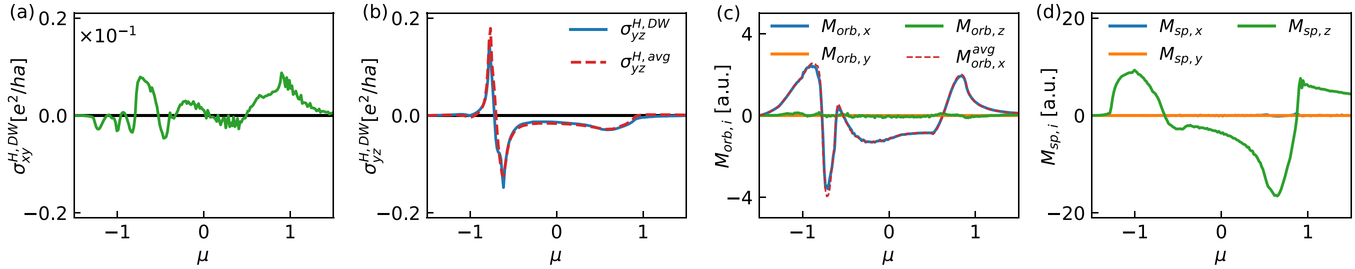

FIG. 6. Anomalous Hall effect and magnetization driven by an altermagnetic domain wall. (a) $\sigma_{xy}^{H,DW}$ vs the chemical potential μ. (b) $\sigma_{yz}^{H,DW}$ vs μ, featuring a nontrivial dependence near $\mu = -0.75$, which is related to the anticrossings along AZ in the bulk band structure in Fig. 4(b). (c) Orbital magnetization induced by the DW vs μ. $\vec{M}_{\rm orb}$ is effectively pointing in the x direction. (d) Spin magnetization induced by the DW vs μ. $\vec{M}_{\rm sp}$ is effectively pointing in the z direction. Therefore, $\vec{M}_{\rm orb}$ and $\vec{M}_{\rm sp}$ are almost perpendicular to each other. The Hall pseudovector $\vec{\sigma}_{H,DW}$, which is effectively along the x axis, is closer related to the orbital magnetization. For the slab geometry, we have chosen $L_x = 100a$ and $w_{\rm dw} = 20a$. The dashed lines in (b) and (c) are obtained from a site averaging, as described in the main text.

with that of $\sigma_{xy}^{H,DW}$. The Hall pseudovector $\vec{\sigma}_{H,DW}$ is thus dominated by its first component, namely $\vec{\sigma}_{H,DW}$ effectively points in the x direction. We also observe a nontrivial μ dependence of $\sigma_{yz}^{H,DW}$, which strongly resembles that in Fig. 5(a). We compare the full result in Fig. 6(b) with a site-averaged Hall conductivity defined by

$$\sigma_{ab}^{H,\text{avg}} = \frac{1}{L_x+1}\sum_{i=-L_x/2}^{L_x/2} \sigma_{ab}^{H}(\vec{N}_i), \tag{7}$$

where $\vec{N}_i$ is the local Néel vector in the ith unit cell of the DW. $\sigma_{ab}^{H}(\vec{N}_i)$ is the Hall conductivity for the collinear bulk with the Néel vector along $\vec{N}_i$. The μ dependence of $\sigma_{yz}^{H}(\vec{N}_i)'$s that enter Eq. (7) can be found in Appendix C.

The result for $\sigma_{yz}^{H,\text{avg}}$ is shown as the dashed line in Fig. 6(b). We find that the site averaging works remarkably well compared with the full calculation. Based on this, one can effectively view the sign-changing behavior of $\sigma_{yz}^{H,DW}$ near $\mu = -0.75$ as the result of band anticrossings akin to the collinear-bulk cases, but here the anticrossings are caused by the DW texture. In general, we expect the site averaging to work better for a smoother DW profile since the DW-induced potential felt by the electrons varies more slowly in space. A notable consequence is that, in a smoother and correspondingly wider DW, there are more unit cells that contribute a nonzero $\sigma_{ab}^{H}(\vec{N}_i)$ in the right-hand side of Eq. (7). In other words, for a fixed L_x, a wider DW with a larger $w_{\rm dw}$ has nonzero contributions from more ith sites in Eq. (7). Consequently, the Hall conductivity is larger. Therefore, DWs with a larger width are expected to induce a larger DW AHE. We note also that the agreement between $\sigma_{yz}^{H,\text{avg}}$ and $\sigma_{yz}^{H,DW}$ provides strong evidence that the Hall effect is indeed activated by the DW, while bulk regions far from the DW do not contribute to the Hall effect, as expected from the altermagnetic symmetry of each domain. Through the definition of $\sigma_{yz}^{H,\text{avg}}$, it is also clear that an experimental setup in which the Hall voltage contacts cover the whole vertical x direction of the slab is needed in order to observe the slab-averaged DW Hall effect given by $\sigma_{yz}^{H,\text{avg}}$ and equivalently the $\sigma_{yz}^{H,DW}$. Next, we study how the DW AHE is related to the orbital and the spin magnetization.

B. Relation to the orbital and spin magnetization

It is instructive to examine a connection between the Hall conductivity and the magnetization. Because of the slab geometry, the expressions for the orbital magnetization and the spin magnetization slightly differ from Eqs. (5) and (6) for the collinear bulk,

$$M_{{\rm sp},i} = -\frac{e\hbar}{2}\frac{1}{L_x+1}\sum_n\int\frac{d^2q}{(2\pi)^2}f(E_{\vec{q}n})\langle u_{\vec{q}n}|\sigma_i|u_{\vec{q}n}\rangle, \tag{8}$$

$$M_{{\rm orb},i} = \frac{e\hbar}{2}\frac{1}{L_x+1}\sum_n\sum_{m\neq n}\int\frac{d^2q}{(2\pi)^2}f(E_{\vec{q}n})(E_{\vec{q}n}+E_{\vec{q}m}-2\mu)i\varepsilon_{ijl}\left[\frac{(v_j)_{\vec{q}}^{nm}(v_l)_{\vec{q}}^{mn}-(v_l)_{\vec{q}}^{nm}(v_j)_{\vec{q}}^{mn}}{(E_{\vec{q}n}-E_{\vec{q}m})^2}\right], \tag{9}$$

where $\vec{q} = \vec{k}_\parallel = (k_y, k_z)$ is the crystal momentum in the plane of the slab, and the jth Cartesian component of the velocity operator v_j is defined in Appendix B.

Figure 6(c) shows the μ dependence of $M_{{\rm orb},i}$ induced by the DW. This result shows that $\vec{M}_{\rm orb}$ points primarily along the x axis. Figure 6(d) illustrates the μ dependence of the spin magnetization $\vec{M}_{\rm sp}$, which is effectively pointing along the z axis. With the same assumption on the effective mass as in the collinear bulk case, we can now compare the order of magnitude between $\vec{M}_{\rm orb}$ and $\vec{M}_{\rm sp}$. Our results show that the orbital magnetization $\vec{M}_{\rm orb}$ is of the same order of magnitude as the spin magnetization $\vec{M}_{\rm sp}$. Moreover, it is clear that the orbital magnetization is a better indicator, compared with the spin magnetization, in terms of which components of the DW Hall pseudovector $\vec{\sigma}_{H,DW}$ are more dominant: the dominant first component of $\vec{M}_{\rm orb}$ correctly indicates that the AHE is

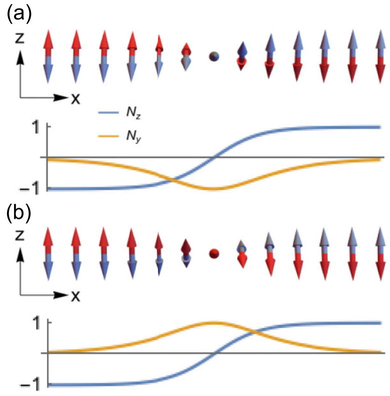

FIG. 7. (a)(b) Time-reversed counterparts of Figs. 3(a) and 3(b), respectively.

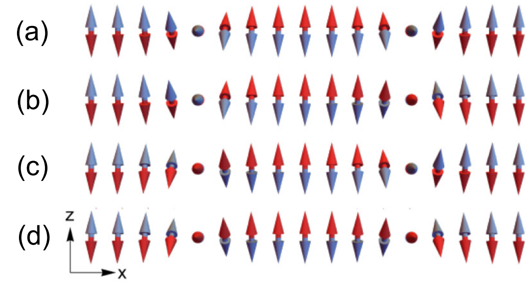

FIG. 8. The four possible DW-pair combinations that are expected to arise in multiple-parallel-DW profiles. They differ by the combination of the sign of N_y at the two DWs. (a) N_y component at the two DWs has (+, +) sign. (b) (+, −) sign. (c) (−, +) sign. (d) (−, −) sign. If an applied magnetic field favors a positive N_y, then the combination (a) has the lowest energy.

strongest in the plane perpendicular to the x axis, namely $\sigma_{yz}^{H,DW}$ dominates over the other components. However, the spin magnetization, which is predominantly in the z direction, incorrectly suggests the dominant $\sigma_{xy}^{H,DW}$ component.

We also find that the spin magnetization exists regardless of the altermagnetism or the SOC. We have checked numerically that the spin magnetization persists even when we set $t_d = \lambda = \lambda' = 0$, which switches off the SOC and the altermagnetism part in the model. In Appendix D, we explain the persistence of $\vec{M}_{\rm sp}$ as arising from the gradient of the Néel vector and the fact that the A and B sublattices are located at slightly different positions, none of which, in contrast to the AHE and the orbital magnetization, require altermagnetism or SOC. Our observation strongly indicates that the orbital magnetization is more closely related to the DW AHE than the spin magnetization, in analogy to the collinear bulk case, where it is the orbital magnetization that provides the dominant contribution to the overall magnetization.

C. Symmetry-imposed relations to other DW profiles

So far, we have discussed the DW AHE for the specific DW illustrated in Fig. 3(a). To obtain the DW AHE for the DW in Fig. 3(b), we execute a z mirror, which is an operation that flips the chirality of (a) and turns it into (b). If we denote the DW Hall conductivity for the DW of type (a) by $\vec{\sigma}_{H,DW} = (\sigma^0_{yz}, \sigma^0_{zx}, \sigma^0_{xy})^T$, then the DW Hall conductivity for type (b) is given by its z-mirror image

$$\left(-\sigma^0_{yz}, -\sigma^0_{zx}, \sigma^0_{xy}\right)^T. \tag{10}$$

There are also time-reversal counterparts of the DW profiles in Fig. 3, which are shown in Fig. 7. Their AHE responses are similarly obtained by implementing a time-reversal operation. Therefore, the Hall pseudovector for the DW profile in Fig. 7(a) is given by

$$\left(-\sigma^0_{yz}, -\sigma^0_{zx}, -\sigma^0_{xy}\right)^T, \tag{11}$$

while that of the DW in Fig. 7(b) is given by

$$\left(\sigma^0_{yz}, \sigma^0_{zx}, -\sigma^0_{xy}\right)^T. \tag{12}$$

D. AHE from mutli-domain-wall profiles

We are ready to discuss the DW AHE in the presence of multiple parallel DWs by examining how the contributions from the constituent DWs may cancel or add up. This depends on which combination of the 4 DW configurations in Figs. 3 and 7 appears; see Fig. 8. For a random combination of a large number of DWs, the contributions are expected to cancel. As will become clear in Sec. IV, it may be possible to apply a magnetic field to select the sign of N_y within the DW region, thereby favoring the pair in Figs. 8(a) or 8(d). As a result, the DW AHE contributions from the constituent DWs add up to a nonzero value. However, the DW AHE is expected to vanish for Figs. 8(b) and 8(c). We also note that $\sigma_{xy}^{H,DW}$ cancels out when combining all configurations in Fig. 8.

Finally, we estimate the order of magnitude of the DW AHE for a profile consisting of parallel DW planes as in either Figs. 8(a) or 8(d) to ensure a nonzero DW AHE. The average separation between neighboring DW planes is inversely proportional to the density of the DW $\rho_{\rm dw}$. The net DW AHE is expected to scale like

$$\sigma_{yz}^{H,DW} L_x \rho_{\rm dw}, \tag{13}$$

where $\sigma_{yz}^{H,DW}$ is the Hall conductivity from the slab-geometry calculation corresponding to the slab thickness L_x and a DW width $w_{\rm dw}$. This is expected to be a good approximation, assuming that the Hall contributions from the constituent DWs do not strongly interfere with one another, and thus these contributions simply add up. We note that the final outcome depends on $\rho_{\rm dw}$ and $w_{\rm dw}$. The latter is intrinsic to each DW, determining the product $\sigma_{yz}^{H,DW} L_x$. This product is expected to converge for a sufficiently large L_x. In other words, we expect the AHE contribution from each DW to be mainly determined by the properties of the DW itself, namely the width $w_{\rm dw}$ in this case. For $L_x = 100a$ and $w_{\rm dw} = 20a$, $\sigma_{yz}^{H,DW}$ is of the order of $10^{-1} e^2/ha$; see Fig. 6(b). For $\rho_{\rm dw} = 1/1000\,a$, i.e., one DW per 1000 lattice constant, the total Hall conductivity is of the order of $10^{-2} e^2/ha$. For $a = 1'$nm, the final value of the Hall conductivity is of the order of magnitude between 1 S/cm and 10 S/cm, which is an appreciable value. Our work reveals a non-negligible role of DWs in understanding Hall transport phenomena in altermagnets, which is particularly crucial for pure altermagnets since the bulk magnetic domains do not support AHE. Therefore, our work generally calls for a careful analysis of the Hall transport data, ideally simultaneously with magnetic imaging data, in order to correctly attribute the observed Hall effect to the bulk magnetic domains or to DWs. In the next section, we return to the demonstration of how an applied magnetic field may indeed select the DW patterns that lead to a nonzero $\sigma_{yz}^{H,DW}$.

IV. INSIGHTS FROM LANDAU THEORY

In this section, we employ Landau theory for rutile altermagnets to explain the qualitative features of our numerical results and to outline a setup in order to achieve a nontrivial DW AHE from multi-DW configurations.

We consider an important aspect of the Landau theory for altermagnets formulated in Refs. [14,47]: coupling between Néel vector $\vec{N}$ and the magnetization $\vec{M}$. They are viewed as order parameters that appear in the free energy for the system. In particular, we are interested in the symmetry-allowed bilinear couplings between the components of $\vec{N}$ and $\vec{M}$. For rutile altermagnets, such a coupling appears as the following Lifshitz invariant [14,17]:

$$L_{\rm int} = \alpha_1(M_xN_y + M_yN_x). \tag{14}$$

α_1 is a coupling constant. We emphasize that this is the only bilinear coupling. Note also that N_z and M_z do not appear at the bilinear order, but they may appear in nonlinear terms. Equation (14) implies that a nonzero M_y (M_x) can be induced by a nonzero N_x (N_y)—the mechanism of weak ferromagnetism discussed earlier [33,41]. Indeed, this explains the emergence of the orbital magnetization $\vec{M}_{\rm orb}$ in Fig. 6(c) from the nonzero N_y component within the DW region [48]. It also explains why the DW gives rise to a nonzero AHE since the Hall pseudovector transforms like a magnetization vector. We note that the Lifshitz invariant of Eq. (14) is not present in Ref. [34] because of the absence of SOC in the study.

Since an external magnetic field $\vec{B}$ also transforms like $\vec{M}$, one can replace $\vec{M}$ in Eq. (14) by $\vec{B}$. This implies that an external magnetic field directly couples to the Néel vector, allowing for control over the DW pattern. For example, a magnetic field in the x direction couples linearly with N_y and will thus energetically favor either the DW pair configuration in Figs. 8(a) or 8(d). This ultimately leads to a nontrivial AHE from DWs, as claimed earlier in Sec. III D. We note that the magnetic domains themselves are less affected by the external magnetic field since the order parameter, i.e., N_z, behaves like a magnetic octupole in the rutile lattice [14,15]. That is, N_z transforms identically as a magnetic octupole moment under the symmetry operations of the point group and couples to the external field, beginning only at the third-order: a Lifshitz invariant of the form $N_zB_xB_yB_z$ is allowed by symmetry [14,15]. Meanwhile, the coupling with the DW chirality already occurs at the linear order.

V. GENERALIZATION BEYOND RUTILE ALTERMAGNETS

So far, we have discussed a specific case of pure rutile altermagnets where AHE is symmetry-forbidden within the interior of each magnetic domain, and how altermagnetic DWs lift the symmetry constraint and activate the AHE. In this section, we discuss how a similar situation can arise in other pure altermagnets. For simplicity, we restrict our attention to pure altermagnets in which it is possible to have a bilinear coupling between $\vec{N}$ and $\vec{M}$ of the following form:

$$L_{\rm int} = \sum_{\alpha,\beta=x,y,z} c_{\alpha\beta}N_\alpha M_\beta, \tag{15}$$

which is a more general version of Eq. (14) for rutiles with coupling constants $c_{\alpha\beta}$. It is expected that the bilinearity of the coupling enables more effective manipulation of the DW configuration by an external field $\vec{B}$, since nonlinear couplings could, in general, lead to reduced controllability, such as requiring a large external field.

We find three crystallographic point groups in three dimensions that support pure altermagnetism and the bilinear couplings simultaneously; see Table I. This table is adapted from a recent work on Landau theories for altermagents [47], and we will describe how to use it in the following. The first column is the crystallographic point group of the underlying lattice. To describe the physical meaning of the second column, we first recall that an altermagnetic ordering does not break the translational symmetry of the lattice. It is instructive to visualize how the staggering dipole moments associated with the Néel order occupy and divide the sublattices in each unit cell into two groups. We define a sign-alternating pattern by assigning the value $+1$ to one group and -1 to the other. It is essential that a translation or an inversion operation does not interchange the sublattices between the two groups in order to avoid the Kramers' degeneracy. Otherwise, we would get conventional antiferromagnetism, i.e., no momentum-dependent band splitting. Nevertheless, the two groups may be interchanged by other operations, e.g., a rotation operation of the crystallographic point group [49]. As a result, such a rotation reverses the sign of the sign-alternating pattern. While some operations of the point group change the sign of the sign-alternating pattern, other operations do not. This means that the sign-alternating pattern transforms according to a one-dimensional irreducible representation of the point group that defines Γ_S. Γ_S varies, depending on the type of Wykoff positions occupied by the sublattices. For rutiles, the point group is $4/mmm$. Within each unit cell, the A sublattice constitutes the first group, while the B sublattice forms the second group. A fourfold rotation is an example that interchanges the two groups. The sign-alternating pattern transforms according to $\Gamma_S = B_{2g}$. Accordingly, the bilinear coupling can be read off from the third column of the table and is indeed given by Eq. (14). Finally, the fourth column specifies the high-symmetry direction for $\vec{N}$ corresponding to the pure altermagnetism. Table I demonstrates the presence of multiple examples of pure altermagnets where bilinear couplings are possible. Our results for the rutile altermagnets can then be readily generalized for these systems.

VI. SUMMARY

Our work demonstrates that in pure altermagnets the symmetry constraint, which forces the AHE to vanish, is lifted by magnetic DWs, thereby activating a DW AHE and orbital

TABLE I. Three-dimensional point groups that can support centrosymmetric pure altermagnetism exhibiting a linear coupling between $\vec{N}$ and $\vec{M}$. Other point groups may support nonlinear coupling beyond the bilinearity. The results are adapted from Ref. [47].

Point group	Staggering Irr. Rep. Γ_S	Lifshitz invariant	$\vec{N}$ in domain interiors
mmm	B_{1g}	$\alpha_1 N_x M_y + \alpha_2 N_y M_x$	along $\hat{z}$
	B_{2g}	$\alpha_1 N_x M_z + \alpha_2 N_z M_x$	along $\hat{y}$
	B_{3g}	$\alpha_1 N_y M_z + \alpha_2 N_z M_y$	along $\hat{x}$
$4/m$	B_g	$\alpha_1(N_x M_x - N_y M_y) + \alpha_2(N_x M_y + N_y M_x)$	along $\hat{z}$
$4/mmm$	B_{1g}	$\alpha_1(N_y M_y - N_x M_x)$	along $\hat{z}$
	B_{2g}	$\alpha_1(N_y M_x + N_x M_y)$	along $\hat{z}$

magnetization. In the presence of many parallel DWs, while a random arrangement of the DW chirality leads to a trivial DW AHE, we argue using Landau theory that an external magnetic field selects a chirality population that allows the AHE contribution from each DW to add up instead of canceling out. Our work also uncovers a crucial role of the orbital magnetization, in that it is comparable to or, in some cases, even larger than the spin magnetization. In addition, its orientation correctly indicates the Hall plane where the DW AHE is the greatest, whereas the spin magnetization fails to do so. Our work calls for experimental investigations to confirm this important role of altermagetic DWs in Hall transport and orbital magnetism phenomena. Because of the important role of DWs in pure altermagnets demonstrated here, future Hall-transport studies should undertake a rigorous analysis of the Hall data, ideally in conjunction with the information about the precise magnetic structure, in order to unambiguously assign an observed Hall effect to the bulk magnetic domains or to the DWs. Our work also motivates future studies of DW effects in mixed altermagnets, where bulk magnetic domains are already AHE-active and accompanied by weak ferromagnetism. It is probable that, in a field-sweep Hall measurement, the Hall contribution from bulk magnetic domains cancels out near the coercive magnetic field, exposing the DW contribution—a scenario proposed in the ferromagnet CeAlSi [38]. Future studies are also needed to firmly establish the dominant effect of orbital magnetism uncovered here in altermagnets. This last point is further reinforced by a similar observation of a dominant orbital magnetism in MnTe in a recent first-principle study [50].

ACKNOWLEDGEMENTS

We thank Markus Garst, Daegeun Jo, and Dongwook Go for very helpful discussions. S.S. is supported by the Deutsche Forschungsgemeinschaft (DFG) through TRR 288 Grant No. 422213477 (Project No. A11). Y.M. acknowledges support by the EIC Pathfinder OPEN Grant No. 101129641 “OBELIX” and No. DFG TRR 173/3—268565370 (Project A11), No. TRR 288/2—422213477 (Project B06).

DATA AVAILABILITY

The data that support the findings of this article are not publicly available. The data are available from the authors upon reasonable request.

APPENDIX A: SYMMETRY PROTECTION OF WEYL NODAL LINES ALONG Γ Z AND MA

In this appendix, we discuss the symmetry protection of the Weyl nodal lines along Γ Z and MA lines seen in the band structure in Fig. 4(b) for the case of a uniform profile $\vec{N} = \hat{y}$. As will be shown below, the Weyl nodal line along MA is protected by a combination of a nonsymmorphic mirror $g_1 = \{\mathcal{M}_x|\frac{1}{2}\frac{1}{2}\frac{1}{2}\}$ and an anti-unitary symmetry $\tilde{g}_2 = \Theta\{C_{2y}|\frac{1}{2}\frac{1}{2}\frac{1}{2}\}$, which involves the time reversal Θ. (Tilde on $\tilde{g}_2$ denotes its anti-unitarity.) Meanwhile, the nodal line along Γ Z is not protected by any symmetry and can be gapped out by a symmetry-conforming pertubation.

To see the absence of a symmetry protection for the nodal line along Γ Z, we supplement the following symmetry-conforming perturbation, which takes the form of a magnetic field along x axis, into the model Hamiltonian $\mathcal{H}$ of Eq. (1),

$$\mathcal{H}_{\text{pert}} = \eta \sigma_x \tau_0, \tag{A1}$$

where η is a coefficient. One can see that $\mathcal{H}_{\text{pert.}}$ is symmetry-allowed from our discussion on the Landau theory for rutile altermagnets, where a Néel vector along y axis induces a weak ferromagnetism with the magnetization along $\underline{x}$ axis. Figure 9(b) shows how introducing $\mathcal{H}_{\text{pert}}$ gaps out the nodal line along Γ Z in Fig. 9(a). In contrast, the Weyl nodal line along MA is still protected.

Below, we outline the reason how g_1 and $\tilde{g}_2$ protect the MA nodal line. One can check that for all k-point along MA, i.e., $\vec{k} = (\pi, \pi, k_z)$, g_1 and $\tilde{g}_2$ are indeed the symmety. Let $\psi_{\vec{k}}$ be an eigenstate and U_1 is the unitary representation of g_1, then

$$\mathcal{H}(\vec{k})\psi_{\vec{k}} = E_{\vec{k}}\psi_{\vec{k}}, \tag{A2}$$

$$[\mathcal{H}(\vec{k}), U_1] = 0, \tag{A3}$$

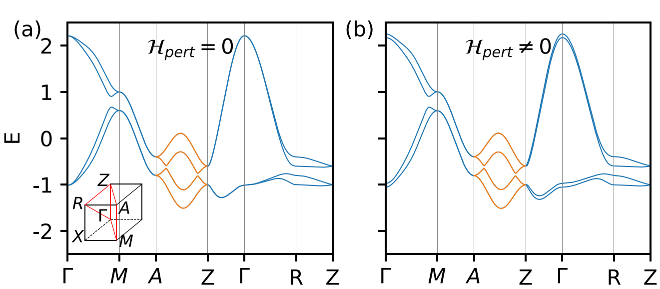

FIG. 9. Demonstration how the symmetry-conforming $\mathcal{H}_{\text{pert}}$ gaps out the nodal line along Γ Z.

$$U_1\psi_{\vec{k}} = \zeta\psi_{\vec{k}}, \tag{A4}$$

where ζ is an eigenvalue of U_1. The square of g_1 is given by

$$g_1^2 = \{e|011\}\{C_{1x}|000\}. \tag{A5}$$

We denote e as identity and C_{1x} as a 2π rotation. This means that ζ depends on $\vec{k}$ and satisfies the following condition:

$$\zeta_{\vec{k}}^2 = -e^{i\pi+ik_z}, \tag{A6}$$

where -1 arises from the 2π rotation of the spin-1/2 electron, while the phase factor comes from the pure translation part of Eq. (A5). This means that $\zeta_{\vec{k}}$ takes two values,

$$\zeta_{\vec{k}} = \pm e^{ik_z/2}. \tag{A7}$$

Next, we consider the relation between g_1 and $\tilde{g}_2$,

$$g_1\tilde{g}_2 = \{e|001\}\{C_{1x}|000\}\tilde{g}_2 g_1. \tag{A8}$$

Let $\tilde{U}_2$ be the anti-unitary representation for $\tilde{g}_2$ and, without loss of generality, let $\zeta_{\vec{k}}$ be $e^{ik_z/2}$, then acting $\tilde{U}_2$ on the following first equation yields

$$U_1\psi_{\vec{k}} = e^{ik_z/2}\psi_{\vec{k}},$$
$$\tilde{U}_2U_1\psi_{\vec{k}} = e^{-ik_z/2}\tilde{U}_2\psi_{\vec{k}}. \tag{A9}$$

We will show that $\tilde{U}_2\psi_{\vec{k}}$ is also an eigenvector of U_1 but with the eigenvalue of $-e^{ik_z/2}$. To see that, we use Eq. (A8),

$$U_1\tilde{U}_2\psi_{\vec{k}} = -e^{ik_z}\tilde{U}_2U_1\psi_{\vec{k}} = -e^{ik_z/2}\tilde{U}_2\psi_{\vec{k}}, \tag{A10}$$

where in the last equality, we use Eq. (A9). This means that $\tilde{U}_2\psi_{\vec{k}}$ is another eigenstate of $\mathcal{H}(\vec{k})$ and carries the opposite g_1 eigenvalue to that of $\psi_{\vec{k}}$. Hence, it is guaranteed that there is a twofold degeneracy protected by g_1 and $\tilde{g}_2$.

APPENDIX B: KUBO FORMULA FOR THE DOMAIN WALL HALL CONDUCTIVITY

The Kubo formula for the Hall conductivity is given by [37]

$$\sigma_{ij}^{H,DW} = \lim_{\omega\to 0}\frac{2\pi i}{L_x+1}\frac{e^2}{h}\sum_{m,n}\int\frac{d^2q}{(2\pi)^2}\frac{f(E_{\vec{q}m})-f(E_{\vec{q}n})}{E_{\vec{q}n}-E_{\vec{q}m}}\left[\frac{(v_i)_{\vec{q}}^{mn}(v_j)_{\vec{q}}^{nm}}{\hbar\omega+i\gamma+E_{\vec{q}m}-E_{\vec{q}n}}\right], \tag{B1}$$

where $\vec{q}=\vec{k}_\parallel=(k_y,k_z)^T$, γ is a small broadening, $|u_{\vec{q}n}\rangle$ denotes the Bloch eigenstates, and v_j is the velocity operator whose matrix elements are defined below.

To obtain the velocity operator, we follow the standard procedure of the Peierls substitution: each hopping term $t_{ij}\psi_i^\dagger\psi_j$ acquires a phase because of the vector potential $\vec{A}$ associated with an external electric field $\vec{E}=-\partial\vec{A}/\partial t$,

$$t_{ij}\psi_i^\dagger\psi_j \to t_{ij}\psi_i^\dagger\psi_j\exp\left(-i\frac{e}{\hbar}\int_{\vec{r}_i}^{\vec{r}_j}d\vec{r}\cdot\vec{A}\right),$$
$$\approx t_{ij}\psi_i^\dagger\psi_j\left[1-i\frac{e}{\hbar}\vec{r}_{ij}\cdot\frac{\vec{A}(\vec{r}_i)+\vec{A}(\vec{r}_j)}{2}\right], \tag{B2}$$

where $\vec{r}_{ij}=\vec{r}_j-\vec{r}_i$. The velocity operator at site i is given by

$$v_l(\vec{r}_i) = -\frac{1}{e}\frac{\delta H[\vec{A}]}{\delta A_l(\vec{r}_i)}, \tag{B3}$$

where $H[\vec{A}]$ is the Hamiltonian after the Peierls substitution. Finally, the velocity operator in Eq. (B1) is given by

$$v_l = \sum_i v_l(\vec{r}_i). \tag{B4}$$

In the rest of the appendix, we will apply our expressions to the case of the slab geometry and sketch the derivation of a useful form of v_l [Eq. (B4)] for the Kubo formula. We will first derive the tight-binding Hamiltonian in the Fourier space and then express v_l in relation to the matrix elements of the Hamiltonian.

The tight-binding Hamiltonian on the slab geometry has the following form:

$$H = \sum_{ii'll'\mu\mu'} t_{il\mu,i'l'\mu'}\psi_{il\mu}^\dagger\psi_{i'l'\mu'} + \text{H.c.}, \tag{B5}$$

where site indices i and i' specify the *in-plane* position. The layer indices l and l' specify the *out-of-plane* position. μ and μ' are compact indices that specify the sublattices and the spin. We note that the position vector consists of out-of-plane and in-plane components: $\vec{r}=(r_\perp,\vec{\mathfrak{r}})$. The in-plane translational invariance is encoded in the hopping integral $t_{il\mu,i'l'\mu'} = t_{l\mu,l'\mu'}(\vec{\mathfrak{r}}_{i'}-\vec{\mathfrak{r}}_i)$, i.e., it depends only on the displacement vector $\vec{\mathfrak{r}}_{i'}-\vec{\mathfrak{r}}_i$ within the slab plane. The Fourier form of H is given by

$$H = \sum_{\vec{q},ll'\mu\mu'}\psi_{\vec{q}l\mu}^\dagger\mathcal{H}_{l\mu,l'\mu'}(\vec{q})\psi_{\vec{q}l'\mu'}, \tag{B6}$$

where

$$\mathcal{H}_{l\mu,l'\mu'}(\vec{q}) = t_{l\mu,l'\mu'}(\vec{q}) + t_{l'\mu',l\mu}^*(\vec{q}), \tag{B7}$$

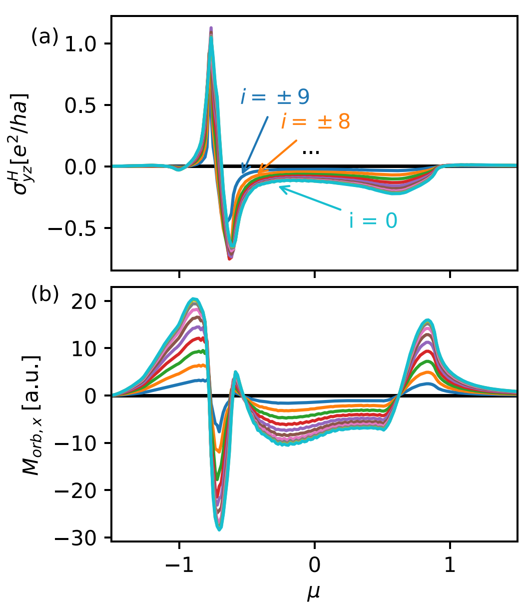

FIG. 10. μ dependence of (a) $\sigma_{yz}^H(\vec{N}_i)$ and (b) $M_{\text{orb},x}(\vec{N}_i)$ for the collinear bulk.

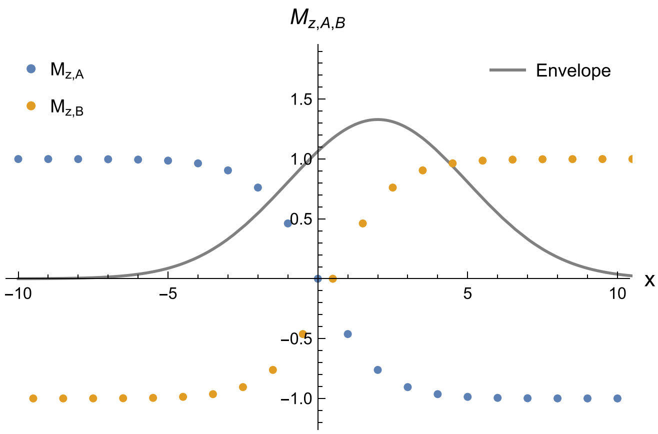

FIG. 11. Profile of $M_{z,A}$ and $M_{z,B}$ near the domain wall. The solid curve illustrates an envelope function for the coarse graining.

$$t_{l\mu,l'\mu'}(\vec{q}) = \sum_{i'} t_{l\mu,l'\mu'}(\vec{\mathfrak{r}}_{ii'})e^{i\vec{q}\cdot\vec{\mathfrak{r}}_{ii'}}, \tag{B8}$$

where $\vec{\mathfrak{r}}_{ii'} = \vec{\mathfrak{r}}_{i'} - \vec{\mathfrak{r}}_i$. We have also used the Fourier transformation

$$\psi_{il\mu} = \frac{1}{\sqrt{A}} \sum_{\vec{q}} \psi_{\vec{q}l\mu} e^{i\vec{q}\cdot\vec{\mathfrak{r}}_i}.$$

A is the area of the slab. The velocity operator Eq. (B4) can be computed similarly. Following Eq. (B4), we can write

$$\vec{v} = \frac{1}{\hbar} \sum_{ii'll'\mu\mu'} it_{il\mu,i'l'\mu'}(r_{\perp,ll'}\hat{x} + \vec{\mathfrak{r}}_{ii'})\psi^{\dagger}_{il\mu}\psi_{i'l'\mu'} + \text{H.c.} \tag{B9}$$

Taking the same Fourier transformation akin to that for the Hamiltonian, we arrive at the following form:

$$v_a = \sum_{\vec{q},ll'\mu\mu'} \psi^{\dagger}_{\vec{q}l\mu}\mathcal{V}^a_{l\mu,l'\mu'}(\vec{q})\psi_{\vec{q}l'\mu'}. \tag{B10}$$

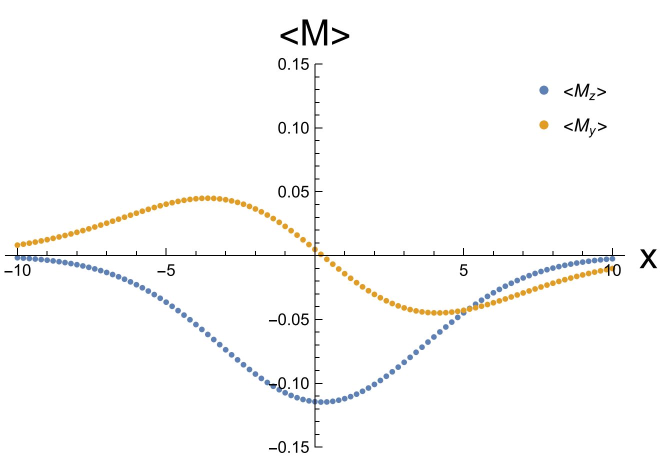

FIG. 12. Profiles of $\langle M_z\rangle$ and $\langle M_y\rangle$ in a DW region. Upon summing over the domain wall region, the z component is nontrivial, while the y component vanishes.

For the in-plane components $a = y, z$,

$$\mathcal{V}^a_{l\mu,l'\mu'}(\vec{q}) = \frac{1}{\hbar}\frac{\partial \mathcal{H}_{l\mu,l'\mu}(\vec{q})}{\partial q_a}, \tag{B11}$$

whereas the out-of-plane component $a = x$ corresponds to

$$\mathcal{V}^x_{l\mu,l'\mu'}(\vec{q}) = \frac{i}{\hbar} r_{\perp,ll'}\mathcal{H}_{l\mu,l'\mu'}(\vec{q}). \tag{B12}$$

Note that there is no summation over the indices l and l' in the right-hand side of the above equation. Finally, the notation for the matrix elements of the velocity operator in Eq. (B4) is given by

$$(v_a)^{mn}_{\vec{q}} = \langle u_{\vec{q}m}|\mathcal{V}^a(\vec{q})|u_{\vec{q}n}\rangle. \tag{B13}$$

APPENDIX C: HALL CONDUCTIVITY AND ORBITAL MAGNETIZATION FOR COLLINEAR BULK

To compute the site-averaged Hall conductivity of Eq. (7) and a similar site-averaged orbital magnetization, we first compute the same quantities for the collinear bulk with the Néel vector orientation $\vec{N}_i$'s that appear in the DW Ansatz for $w_{\text{dw}} = 20$. Recall that $\vec{N}_i = (0, \sin\theta_i, \cos\theta_i)^T$ and $\theta_i = \pi(2i + w_{\text{dw}})/2w_{\text{dw}}$ in the DW region $-w_{\text{dw}}/2 < i < w_{\text{dw}}/2$. Figure 10 shows the μ dependence of the Hall conductivity $\sigma^H_{yz}(\vec{N}_i)$ and that of the orbital magnetization $M_{\text{orb},x}(\vec{N}_i)$. Note that $\vec{N}_{i=0} = \hat{y}$.

APPENDIX D: NONALTERMAGNETIC ORIGIN OF SPIN MAGNETIZATION

In this appendix, we illustrate how the z component of the spin magnetization does not require altermagnetism. This can be seen by observing that the magnetic moments on the two sublattices reside at different positions, i.e., within each unit cell the sublattices A and B are located at different positions. As a result, a coarse graining of a Bloch DW profile of the Néel vector can qualitatively explain the nonvanishing spin magnetization. This arises independently of altermagnetism or spin-orbit coupling.

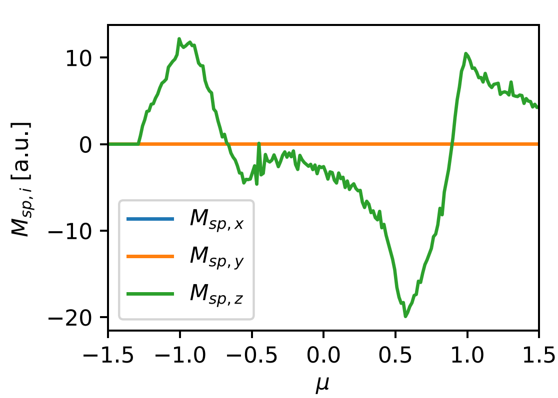

FIG. 13. Spin magnetization of conduction electrons in the absence of altermagnetism and SOC, i.e., when $t_d = \lambda = \lambda' = 0$. The presence of the z component of $\vec{M}_{\text{sp}}$ indeed does not rely on the altermagnetism or SOC, which is in agreement with the coarse graining picture in Fig. 12.

We start by considering a Bloch domain wall of $\vec{N}$ as studied in the main text. Figure 11 shows the profiles of the associated magnetic dipole moments of the sublattices A and B. Without loss of generality, we only consider their z components. We then perform a coarse graining procedure to obtain an averaged local magnetization

$$\langle \vec{M} \rangle(x) = \sum_i \sum_{s=A,B} f(x - x_i)\vec{M}_s(x_i), \quad \text{(D1)}$$

where i is the unit-cell label, and $f(x - x_i)$ is an envelope function peaking at around $x - x_i = 0$. The solid curve in Fig. 11 illustrates a Gaussian envelope function. We note that $\langle \vec{M} \rangle$ should be viewed as a proxy for the spin magnetization studied in the main text.

Performing the coarse graining, we obtain the profile for the z component as shown in Fig. 12. We can also repeat the same calculation for the y component. Upon summing over the DW region, only the z component survives. This means that the DW profile of the Néel vector generally produces a nontrivial magnetization, and it relies on neither altermagnetism nor spin-orbit coupling; the same outcome arises in a conventional antiferromagnet. To illustrate the last point, we compute the spin magnetization when we switch off altermagnetism and spin-orbit coupling, i.e., by setting $t_d = \lambda = \lambda' = 0$. Figure 13 shows the μ dependence of $\vec{M}_{sp}$ and is to be compared with Fig. 6(d) in the main text. The presence of z component of $\vec{M}_{sp}$ indeed does not rely on altermagnetism or spin-orbit coupling, and its value is qualitatively similar to that in Fig. 6(d).

[1] L. Šmejkal, J. Sinova, and T. Jungwirth, Beyond conventional ferromagnetism and antiferromagnetism: A phase with nonrelativistic spin and crystal rotation symmetry, Phys. Rev. X **12**, 031042 (2022).

[2] L. Šmejkal, J. Sinova, and T. Jungwirth, Emerging research landscape of altermagnetism, Phys. Rev. X **12**, 040501 (2022).

[3] L. Bai, W. Feng, S. Liu, L. Šmejkal, Y. Mokrousov, and Y. Yao, Altermagnetism: Exploring new frontiers in magnetism and spintronics, Adv. Funct. Mater. **34**, 2409327 (2024).

[4] Y. Noda, K. Ohno, and S. Nakamura, Momentum-dependent band spin splitting in semiconducting MnO_2: A density functional calculation, Phys. Chem. Chem. Phys. **18**, 13294 (2016).

[5] K.-H. Ahn, A. Hariki, K.-W. Lee, and J. Kuneš, Antiferromagnetism in RuO_2 as d-wave pomeranchuk instability, Phys. Rev. B **99**, 184432 (2019).

[6] S. Hayami, Y. Yanagi, and H. Kusunose, Momentum-dependent spin splitting by collinear antiferromagnetic ordering, J. Phys. Soc. Jpn. **88**, 123702 (2019).

[7] M. Naka, S. Hayami, H. Kusunose, Y. Yanagi, Y. Motome, and H. Seo, Spin current generation in organic antiferromagnets, Nat. Commun. **10**, 4305 (2019).

[8] S. Hayami, Y. Yanagi, and H. Kusunose, Bottom-up design of spin-split and reshaped electronic band structures in antiferromagnets without spin-orbit coupling: Procedure on the basis of augmented multipoles, Phys. Rev. B **102**, 144441 (2020).

[9] R. M. Fernandes, V. S. de Carvalho, T. Birol, and R. G. Pereira, Topological transition from nodal to nodeless Zeeman splitting in altermagnets, Phys. Rev. B **109**, 024404 (2024).

[10] C. Ederer and N. A. Spaldin, Towards a microscopic theory of toroidal moments in bulk periodic crystals, Phys. Rev. B **76**, 214404 (2007).

[11] N. A. Spaldin, M. Fiebig, and M. Mostovoy, The toroidal moment in condensed-matter physics and its relation to the magnetoelectric effect, J. Phys.: Condens. Matter **20**, 434203 (2008).

[12] Y. Kuramoto, H. Kusunose, and A. Kiss, Multipole orders and fluctuations in strongly correlated electron systems, J. Phys. Soc. Jpn. **78**, 072001 (2009).

[13] P. Santini, S. Carretta, G. Amoretti, R. Caciuffo, N. Magnani, and G. H. Lander, Multipolar interactions in f-electron systems: The paradigm of actinide dioxides, Rev. Mod. Phys. **81**, 807 (2009).

[14] P. A. McClarty and J. G. Rau, Landau theory of altermagnetism, Phys. Rev. Lett. **132**, 176702 (2024).

[15] S. Bhowal and N. A. Spaldin, Ferroically ordered magnetic octupoles in d-wave altermagnets, Phys. Rev. X **14**, 011019 (2024).

[16] C. R. W. Steward, R. M. Fernandes, and J. Schmalian, Dynamic paramagnon-polarons in altermagnets, Phys. Rev. B **108**, 144418 (2023).

[17] D. S. Antonenko, R. M. Fernandes, and J. W. F. Venderbos, Mirror chern bands and Weyl nodal loops in altermagnets, Phys. Rev. Lett. **134**, 096703 (2025).

[18] S. Sorn, Antichiral surface states and Su-Schrieffer-Heeger physics in rutile altermagnets, Phys. Rev. B **111**, L161109 (2025).

[19] X. Zhou, W. Feng, R.-W. Zhang, L. Šmejkal, J. Sinova, Y. Mokrousov, and Y. Yao, Crystal thermal transport in altermagnetic RuO_2, Phys. Rev. Lett. **132**, 056701 (2024).

[20] S. Sorn and A. S. Patri, Signatures of hidden octupolar order from nonlinear Hall effects, Phys. Rev. B **110**, 125127 (2024).

[21] Y. Fang, J. Cano, S. Ali, and A. Ghorashi, Quantum geometry induced nonlinear transport in altermagnets, Phys. Rev. Lett. **133**, 106701 (2024).

[22] J. Ōiké, K. Shinada, and R. Peters, Nonlinear magnetoelectric effect under magnetic octupole order: Application to a d-wave altermagnet and a pyrochlore lattice with all-in/all-out magnetic order, Phys. Rev. B **110**, 184407 (2024).

[23] T. Farajollahpour, R. Ganesh, and K. V. Samokhin, Light-induced charge and spin Hall currents in materials with C4K symmetry, npj Quantum Mater. **10**, 29 (2025).

[24] K. V. Yershov, V. P. Kravchuk, M. Daghofer, and J. van den Brink, Fluctuation-induced piezomagnetism in local moment altermagnets, Phys. Rev. B **110**, 144421 (2024).

[25] K. Takahashi, C. R. W. Steward, M. Ogata, R. M. Fernandes, and J. Schmalian, Elasto-Hall conductivity and the anomalous Hall effect in altermagnets, Phys. Rev. B **111**, 184408 (2025).

[26] L. Šmejkal, R. González-Hernández, T. Jungwirth, and J. Sinova, Crystal time-reversal symmetry breaking and spontaneous Hall effect in collinear antiferromagnets, Sci. Adv. **6**, eaaz8809 (2020).

[27] R. P. Rao, R. C. Sherwood, and N. Bartlett, "Weak" ferromagnetism in PDF, J. Chem. Phys. **49**, 3728 (1968).

[28] Z. H. Zhu, J. Strempfer, R. R. Rao, C. A. Occhialini, J. Pelliciari, Y. Choi, T. Kawaguchi, H. You, J. F. Mitchell, Y. Shao-Horn, and R. Comin, Anomalous antiferromagnetism in metallic RuO_2 determined by resonant x-ray scattering, Phys. Rev. Lett. **122**, 017202 (2019).

[29] Z. Feng, X. Zhou, L. Šmejkal, L. Wu, Z. Zhu, H. Guo, R. González-Hernández, X. Wang, H. Yan, P. Qin *et al.*, An anomalous Hall effect in altermagnetic ruthenium dioxide, Nat. Electron. **5**, 735 (2022).

[30] L. Šmejkal, A. H. MacDonald, J. Sinova, S. Nakatsuji, and T. Jungwirth, Anomalous Hall antiferromagnets, Nat. Rev. Mater. **7**, 482 (2022).

[31] M. Wang, K. Tanaka, S. Sakai, Z. Wang, K. Deng, Y. Lyu, C. Li, D. Tian, S. Shen, N. Ogawa, N. Kanazawa, P. Yu, R. Arita, and F. Kagawa, Emergent zero-field anomalous Hall effect in a reconstructed rutile antiferromagnetic metal, Nat. Commun. **14**, 8240 (2023).

[32] K. P. Kluczyk, K. Gas, M. J. Grzybowski, P. Skupinski, M. A. Borysiewicz, T. Fas, J. Suffczynski, J. Z. Domagala, K. Grasza, A. Mycielski, M. Baj, K. H. Ahn, K. Vyborny, M. Sawicki, and M. Gryglas-Borysiewicz, Coexistence of anomalous Hall effect and weak magnetization in a nominally collinear antiferromagnet MnTe, Phys. Rev. B **110**, 155201 (2024).

[33] D. Jo, D. Go, Y. Mokrousov, P. M. Oppeneer, S.-W. Cheong, and H.-W. Lee, Weak ferromagnetism in altermagnets from alternating g-tensor anisotropy, Phys. Rev. Lett. **134**, 196703 (2025).

[34] O. Gomonay, V. P. Kravchuk, R. Jaeschke-Ubiergo, K. V. Yershov, T. Jungwirth, L. Šmejkal, J. van den Brink, and J. Sinova, Structure, control, and dynamics of altermagnetic textures, npj Spintronics **2**, 35 (2024).

[35] W. Xia, B. Bai, X. Chen, Y. Yang, Y. Zhang, J. Yuan, Q. Li, K. Yang, X. Liu, Y. Shi, H. Ma, H. Yang, M. He, L. Li, C. Xi, L. Pi, X. Lv, X. Wang, X. Liu, S. Li *et al.*, Giant domain wall anomalous Hall effect in a layered antiferromagnet $EuAl_2Si_2$, Phys. Rev. Lett. **133**, 216602 (2024).

[36] F. R. Lux, F. Freimuth, S. Blügel, and Y. Mokrousov, Chiral Hall effect in noncollinear magnets from a cyclic cohomology approach, Phys. Rev. Lett. **124**, 096602 (2020).

[37] S. Sorn and A. Paramekanti, Domain wall skew scattering in ferromagnetic Weyl metals, Phys. Rev. B **103**, 104413 (2021).

[38] M. M. Piva, J. C. Souza, V. Brousseau-Couture, S. Sorn, K. R. Pakuszewski, J. K. John, C. Adriano, M. Côté, P. G. Pagliuso, A. Paramekanti, and M. Nicklas, Topological features in the ferromagnetic Weyl semimetal CeAlSi: Role of domain walls, Phys. Rev. Res. **5**, 013068 (2023).

[39] In the mixed altermagnetic cases, incorporating weak ferromagnetism can lead to a slight deviation from a perfect collinearity. In that case, the term "collinear" refers to the collinearity of the sublattice exchange terms that enter the tight-binding Hamiltonian.

[40] M.è Roig, A. Kreisel, Y. Yu, B. M. Andersen, and D. F. Agterberg, Minimal models for altermagnetism, Phys. Rev. B **110**, 144412 (2024).

[41] T. Adamantopoulos, M. Merte, F. Freimuth, D. Go, L. Zhang, M. Ležaić, W. Feng, Y. Yao, J. Sinova, L. Šmejkal, S. Blügel, and Y. Mokrousov, Spin and orbital magnetism by light in rutile altermagnets, npj Spintronics **2**, 46 (2024).

[42] T. Thonhauser, D. Ceresoli, D. Vanderbilt, and R. Resta, Orbital magnetization in periodic insulators, Phys. Rev. Lett. **95**, 137205 (2005).

[43] D. Xiao, J. Shi, and Q. Niu, Berry phase correction to electron density of states in solids, Phys. Rev. Lett. **95**, 137204 (2005).

[44] D. Ceresoli, T. Thonhauser, D. Vanderbilt, and R. Resta, Orbital magnetization in crystalline solids: Multi-band insulators, chern insulators, and metals, Phys. Rev. B **74**, 024408 (2006).

[45] J. Shi, G. Vignale, D. Xiao, and Q. Niu, Quantum theory of orbital magnetization and its generalization to interacting systems, Phys. Rev. Lett. **99**, 197202 (2007).

[46] The effective mass of the electrons is of the order of $\hbar^2/a^2W$, where W denotes the bandwidth, and a is the lattice constant. This means that one can vary the tight-binding parameters in order to change W and the effective mass. Assuming the unit where $\hbar = a = m_e = 1$, the bandwidth W as seen in Fig. 4 produces the effective mass comparable with the bare mass m_e. Therefore, we can indeed compare the order of magnitude between $\vec{M}_{\text{orb}}$ and $\vec{M}_{\text{sp}}$ with the choice of the tight-binding parameters.

[47] H. Schiff, P. McClarty, J. G Rau, and J. Romhanyi, Collinear altermagnets and their Landau theories, Phys. Rev. Res. **7**, 033301 (2025).

[48] The origin of the x component of $\vec{M}_{\text{sp}}$ can also be understood this way, but the spin magnetization is dominated by the nonrelativistic contribution, i.e., the x component is masked by the z component that has a nonrelativistic and a non-altermagnetic origin, as discussed in the Appendix D. For this reason, the Landau theory appears less relevant for $\vec{M}_{\text{sp}}$.

[49] In practice, one needs to consider symmetry operations of the *space* group, but each of such operations can be identified unambiguously with an operation of the point group.

[50] C. Chen Ye, K. Tenzin, J. Slawińska, and C. Autieri, Dominant orbital magnetization in the prototypical altermagnet MnTe, arXiv:2505.08675.